Received: 3 November 2022 | Revised: 8 November 2023 | Accepted: 17 November 2023

DOI: 10.1002/joc.8320

RESEARCH ARTICLE

International Journal of Climatology RMetS

Pattern scaling the parameters of a Markov-chain gamma-distribution daily precipitation generator

Sarah Wilson Kemsley[1] | **Timothy J. Osborn**[1] | **Stephen R. Dorling**[2] | **Craig Wallace**[3]

[1]Climatic Research Unit, School of Environmental Sciences, University of East Anglia, Norwich, UK

[2]School of Environmental Sciences, University of East Anglia, Norwich, UK

[3]EarthSystemData Ltd, The Enterprise Centre, Norwich, UK

Correspondence
Sarah Wilson Kemsley, Climatic Research Unit, School of Environmental Sciences, University of East Anglia, Norwich NR4 7TJ, UK.
Email: s.wilson-kemsley@uea.ac.uk

Funding information
Atkins Ltd.; Natural Environment Research Council, Grant/Award Number: NE/S007334/1

Abstract

General circulation models (GCMs) are the most sophisticated tools at our disposal for studying future climates, but there are limitations to overcome. These include resolutions that may be too coarse for impact assessments, limited or zero availability of some policy-relevant scenarios, and limited time-series length for assessing the risk of extreme events. We illustrate how these limitations can be addressed by combining a stochastic precipitation generator (SPG) with pattern scaling (PS) of its key parameters. Computationally inexpensive, SPG parameters can be perturbed to generate time-series representative of weather under a future climate with high spatial and temporal resolution. If the SPG parameter perturbations are derived directly from GCM simulations projections can only be made for scenarios already simulated by the GCM. Instead, we obtain the parameter perturbations using PS, facilitating emulation of scenarios not necessarily explicitly simulated by the GCM, and where we scale perturbations approximately linearly with global temperature change. PS is commonly applied to estimate perturbations in the mean of climate variables, but rarely to higher-order parameters as we demonstrate here. We apply PS for the first time, globally, to the parameters of a daily, first-order Markov-chain gamma-distribution SPG using output from the IPSL-CM6A-LR GCM to perturb an SPG fitted to observed data from two stations in diverse climates (Santarém, Brazil and Reykjavik, Iceland) to illustrate this novel approach. We produce time series corresponding to a range of GWLs and demonstrate the capability of the combined SPG-PS approach to study local-scale, future daily precipitation characteristics, climate and subsequent risk of extreme weather events.

KEYWORDS

climate modelling, global, pattern scaling, precipitation, stochastic weather generator

1 | INTRODUCTION

General circulation models (GCMs) are the most sophisticated and widely utilized tools used to study the climate's response to external forcings. However, GCM outputs may not be directly suitable for impact assessments due to their coarse resolution (Mitchell, 2003) or, in cases where the resolution is suitable (e.g., High Res MIP; Haarsma et al., 2016), by a limitation in the number of simulations inadequately separating the climate change

signal from unforced variability. Several methods have been discussed in the literature to address the mismatch between GCM area-averaged outputs and the local-scale resolutions required for hydrological, agricultural and ecological assessments, including statistical and dynamical downscaling techniques (Maraun et al., 2010). Stochastic weather generators (SWGs) are tools that have been used to statistically downscale GCM outputs and produce long time series for a range of weather variables at a local-scale (Jones et al., 2016; Wilks, 1999, 2010). Weather generator parameters are typically estimated using a local observed record, and then projected changes in parameters can be diagnosed from GCM simulations for a *specific* scenario and/or time period. While this addresses the resolution mismatch, it can only be applied to scenarios or time periods presently simulated by the GCM. Although a defined range of climate scenarios have been considered by the sixth Coupled Model Intercomparison Project (CMIP6) GCMs, including mitigated, weak and high forcing scenarios, there is no quantification of each scenario's likelihood (Tebaldi et al., 2021; van Vuuren et al., 2011) and therefore the study of a handful of scenarios alone does not capture the range of uncertainty.

Pattern scaling (PS) addresses the issue of limited simulations. Originally developed to create transient projections from equilibrium responses of a GCM to doubled CO_2 concentration (Santer et al., 1990), PS has recently been used to construct projections for scenarios and time periods where fully coupled projections are not available, and thus better understand uncertainty (Lynch et al., 2017; Osborn et al., 2016; Tebaldi & Arblaster, 2014). This approach has also been applied within the IPCC Sixth Assessment Report (IPCC, 2021). Computationally inexpensive, PS typically relies upon a linear relationship to approximate the local climate change (e.g., within a grid cell), via the global mean surface temperature (GMST). Osborn et al. (2016, 2018) argued that this linear approximation does not need to be perfect but that, to be useful, errors arising from this approximation should be small relative to the other sources of uncertainty (e.g., relative to the spread of results in an ensemble of different GCMs). A spatial pattern of this relationship is derived from transient GCM data expressed in a normalized way, for instance, as change per degree Celsius of GMST change. The resulting pattern can hence be scaled by a specific GMST change or a time series of GMSTs, to emulate the climate at a specified global warming level (GWL).

The raw GCM data used to define the spatial patterns are usually composed of monthly or seasonal means, and are typically time filtered (e.g., a multiyear running average) to clarify the external forcing signal. As a result, further treatment of the PS output is needed to investigate extreme events at different time scales (e.g., daily events), and while variability responses (e.g., interannual variability) are sometimes scaled (e.g., Osborn et al., 2016) they are not routinely accounted for despite their importance (Katz & Brown, 1992; Seneviratne et al., 2021).

SWGs are frequently used to produce time series for a range of weather variables in the absence of high quality, consistent records for use in hydrological and agricultural risk assessments (Semenov et al., 1998). Long, synthetic time series also allow for more accurate estimation of the probabilities of extreme events, such as long wet or dry spells, where observed records may be too short (Furrer & Katz, 2008; Semenov & Barrow, 2002; Senemov, 2008). SWGs are computationally inexpensive and can produce several realizations of the climate that they have been calibrated to. However, unlike GCMs, SWGs do not represent the physical processes that determine the climate change induced by external forcing. This means that they cannot, on their own, be used to produce realizations of the future climate without some perturbation as input. Instead, changes in their parameters need to be provided by an external source (such as diagnosing changes from GCM or regional climate model [RCM] simulations).

This study, therefore, applies PS to the first-order transition probabilities and wet-day gamma parameters of a stochastic *precipitation* generator (SPG, defined in section 2) generating long time series that are representative of presently unmodelled GCM–scenario combinations, while also addressing issues regarding coarse GCM resolution and reducing the impact of GCM-induced biases in the projection of local scale climates. To demonstrate this approach, global gridded transition probability and gamma parameter responses to external forcings will be diagnosed using the IPSL-CM6A-LR GCM (Boucher et al., 2020). The implications of the response patterns to resultant precipitation will briefly be interpreted and compared to CMIP5/6 projected trends in precipitation with changing GMST. Finally, the response patterns will be used to perturb transition probabilities and gamma parameters calculated from weather station observations at Santarém, Brazil and Reykjavik, Iceland, and generate precipitation occurrence under a range of global warming levels (GWLs).

2 | DATA AND METHODS

2.1 | Selection of climate scenarios and GCMS

A wide range of future forcing pathways are covered by the CMIP6 ScenarioMIP "Tier 1" experiments, from strongly mitigated (i.e., SSP1-2.6) to high end forcing (i.e., SSP5-8.5) scenarios (O'Neill et al., 2016; Riahi et al., 2017; Tebaldi et al., 2021). Three of the four experiments (SSP1-2.6, SSP2-4.5 and SSP5-8.5) are analogous to CMIP5

experiments, studying similar radiative forcings by 2100 (corresponding to RCPs 2.6, 4.5 and 8.5). SSP3-7.0 has been constructed to fill a gap between medium (SSP2-4.5) and high (SSP5-8.5) pathways (Tebaldi et al., 2021). Weaker forcing or strongly mitigated scenarios are known to produce less well-defined response patterns, which, when extrapolated, lack characteristics present in higher forcing responses. Strongly mitigated scenarios are also thought to show nonlinear precipitation changes (Wu et al., 2010) with the spatial characteristics of warming changing as deep ocean temperatures gradually approach equilibrium (May, 2012). While it is possible to extrapolate patterns from low-end warming scenarios, it has been recommended that patterns should instead be diagnosed from strong forcing scenarios (Mitchell, 2003) and it has been shown that response patterns diagnosed *excluding* high-end scenarios may perform poorly beyond certain GWLs (Osborn et al., 2018). Therefore, only the high-end forcing scenarios, SSP3-7.0 and SSP5-8.5, will be used to produce climate response patterns in this study. Furthermore, the pooling of two SSPs provides a larger sample size, thus improving the signal-to-noise ratio of the forced response against internal climate variability (Osborn et al., 2018).

While any GCM could have been chosen (since this is a proof-of-concept) we select IPSL-CM6A-LR on account of two reasons. First, it has an initial condition ensemble of runs ($n = 4$) for both SSPs which allows more accurate climate change patterns to be diagnosed when the signal-to-noise ratio is small (Mitchell, 2003). Second, it has a moderate-to-high climate response; the GMST change by 2100 slightly exceeds the "very likely" ranges assessed by AR6 (IPCC, 2021) and its equilibrium climate sensitivity is 4.5°C, which lies towards the upper end of AR6 assessed range. These characteristics ensure good coverage of GMST space when deriving the scaling coefficients required for PS. The intermodel spread of responses is likely to be larger than errors within a GCM (Osborn et al., 2016; Tebaldi & Arblaster, 2014) but quantifying that is not the focus of this study.

Four initial condition ensemble members for both the SSP5-8.5 and SSP3-7.0 ScenarioMIP experiments and historical CMIP6 simulations will be used to diagnose the spatial response of first-order Markov probabilities. Historical simulations cover the 1850–2015 period, and ScenarioMIP simulations 2015–2100. Each realization has unique, internally generated variations independent of the forced climate signal which remains constant between realizations. The components of unforced variability in the ensemble members are independent of each other (Jones et al., 2011); thus, it can be expected that pooling four ensemble members will reduce the size of the internal, unforced variability by half relative to using a single member (Osborn et al., 2018).

Historical simulations have been concatenated with the corresponding ScenarioMIP realizations to produce a temporally consistent series from 1850 to 2100. For example, the first realizations of SSP3-7.0 and SSP5-8.5 have been concatenated with the first realization of the historical simulation. The concatenated time series will hereafter be referred to as historical+SSP3-7.0 and historical+SSP5-8.5. The four historical+SSP3-7.0 and four historical+SSP5-8.5 ensemble members will be pooled, resulting in eight temporally consistent time series covering 1850–2100.

2.2 | Determining the spatial response patterns

First-order, two-state Markov chains are frequently used to stochastically simulate daily precipitation occurrence (Richardson & Wright, 1984), where two-state refers to the precipitation status of a day, that is, either wet or dry, with "wet" here defined as a precipitation amount of at least 0.1 mm. While a higher number of states may be beneficial for some applications, here we use two-state. Increasing the number of states adds complexity in defining thresholds and requires the fitting of additional precipitation distributions for each additional state. Following the generation of a binary number sequence representing wet or dry days, Markov-chain weather generators typically attribute an amount of precipitation to a wet day by sampling independently from a two-parameter gamma distribution, fitted monthly. While higher-order models have merits, first-order Markov chains are the most commonly used (Jimoh & Webster, 1996; Schoof & Pryor, 2008), and in a global comparison of zeroth, first, second, and third model-order performance, Wilson Kemsley et al. (2021) showed that first-order models are the most accurate at reproducing observed distributions of wet-spell length. For this reason, first-order Markov chains only will be considered here.

First-order transition probabilities, required by the first-order Markov chain, are defined as

$$P_{ij} = \frac{n_{ij}}{\sum_{m=0}^{1} n_{im}}, \tag{1}$$

where i and j represent wet (1) or dry (0) days and n_{ij} the number of days in the observed record corresponding to the precipitation state defined by i and j on the preceding and current day, respectively. Transition probabilities are calculated for each of the 12 calendar months, resulting in four probabilities per month: P_{11} (a wet day preceding a wet day), P_{00} (a dry day preceding a dry day), P_{01} (a dry day preceding a wet day) and P_{10} (a wet day preceding a dry day), though the number of independent transition probabilities is only two per month because $P_{11} = 1 - P_{10}$. Change patterns for P_{00} and P_{11} will be presented here.

The response of first-order transition probabilities and wet-day gamma parameters to changing GMST will be diagnosed from IPSL-CM6A-LR. For a given month, the change in a transition probability, P, at a GCM grid-cell x, y, will be regressed using least squares regression against the GMST change relative to 1850–1900, such that

$$P_{xyn} - P_{xy,n=0} = a_{P_{xy}}(T_n - T_{n=0}) + c_{P_{xy}}, \quad (2)$$

where n is any 30-year window and with $n=0$ referring to the first 30-year window used to calculate parameters. The gradients plotted globally form the spatial response pattern for each transition probability. The full historical+SSP3-7.0 time series will be used in the regression, but only the responses diagnosed from 2015 to 2100 of the historical+SSP5-8.5 time series will be considered to avoid duplication of responses diagnosed from the historical simulation. This results in four ensemble members each of historical and SSPs 3–7.0 and 5–8.5 used in the determining the response.

Linear regression on the full time series has been used over a simple time-slice (or "delta-change") method. The time-slice approach is more sensitive to random noise caused by internal variability while regression uses the full simulated time series reducing the influence of internal variability (Ruosteenoja et al., 2007) and avoids dependence on the choice of the epoch of the slices (Lynch et al., 2017).

The response of wet-day gamma-distribution parameters to changing GMST is determined as a fractional change (Osborn, 1997; Osborn et al., 2016). The shape (α) and scale (β) parameters for days where the precipitation exceeds 0.1 mm are similarly calculated from 30-year windows every 5 years from 1850 to 2100 using the historical+SSP3-7.0 and historical+SSP5-8.5 time series for each month. Shape and scale parameters are calculated using the Thom estimators

$$\alpha = \frac{1 + \left(1 + \frac{4D}{3}\right)^{\frac{1}{2}}}{4D}, \quad (3)$$

$$\beta = \frac{\overline{x}}{\alpha}, \quad (4)$$

with sample statistic

$$D = \ln(\overline{x}) - \frac{1}{n}\sum_{i=1}^{n} \ln(x_i), \quad (5)$$

where x is the precipitation on wet day i, with a total of n wet days. Thom estimators make better use of the information in a dataset and are considered more efficient than moment estimators (Wilks, 2011).

Although PS is typically applied to mean climate, Osborn et al. (2016) applied PS to *monthly* precipitation *shape* parameters—that, together with the mean precipitation change—determines the distribution of monthly total precipitation. Similar methodology will be applied here, though to *daily* wet-day shape and scale parameters instead. Gamma distributions have been shown to approximate daily precipitation amounts with good accuracy in several studies, both within and outside stochastic weather generator literature (e.g., Chen & Brissette, 2014; Groisman et al., 1999; Martinez-Villalobos & Neelin, 2019; Semenov & Bengtsson, 2002; Wilby & Wigley, 2002). It should be noted that in some locations, seasons, or precipitation regimes, a gamma distribution may not be the closest approximation to the true distribution. In a comparison of eight different distributions, Chen and Brissette (2014) found that compound distributions, such as the mixed-exponential, capture extreme daily precipitation better than single distributions (such as gamma). However, they found that single distributions are instead more suited for climate *change* adaptations than the more complex compound distributions, owing to their structural simplicity. Therefore, due to its flexibility using only two parameters, gamma was one of three distributions recommended for climate change studies (Chen & Brissette, 2014), which in turn makes it a good candidate for PS. For these reasons, we follow the established frameworks of Osborn et al. (2016) and others here, demonstrating the application of PS to *daily* shape and scale parameters.

Fractional changes to these parameters, referred to collectively as W, are regressed against the change in GMST anomaly (relative to 1850–1900) for each GCM grid cell x,y, such that

$$\frac{W_{xyn}}{W_{xy,n=0}} = a_{W_{xy}}(T_n - T_{n=0}) + c_{Wxy}, \quad (6)$$

where n corresponds to the nth 30-year period and $n=0$ once again refers to the first 30-year period with a calculated parameter. $W_{xy,n=0}$ is averaged across all ensemble members in the first recorded 30-year window (usually 1850–1880) where possible. However, some grid cells may have limited or no wet days during a given month over the first (or any) 30-year period making an estimation of the wet-day gamma distribution challenging or impossible. If, in a given month for any 30-year period, there are less than 30 wet days (i.e., one per month), no parameters will be recorded. If this happens to be in the first 30-year window (i.e., 1850–1880), $W_{xy,n=0}$ in Equation (6) is instead the *first* 30-year period that contains a calculated gamma parameter. This may be averaged across all ensemble members (if all of them contain recordings in the same 30-year window) or just one ensemble member. The

corresponding $T_{n=0}$ in Equation (6) will be calculated from the same 30-year period as $W_{n=0}$.

Unlike the transition probabilities, this may result in some locations and months containing fewer data points for regression. If there are less than 10 recordings of W_{xyn} across all simulations (i.e., at least 10 points in the regression), it is determined that there is not enough data to robustly identify a change in the parameter with changing GMST, and thus the slope $a_{W_{xy}}$, for a given month and grid cell, is set to zero. This is a conservative choice; in the absence of robust information about the projected change, we assume no change.

2.3 | Application of the spatial response patterns

The GCM-diagnosed responses of transition probabilities can be utilized by a SPG to produce local scale, daily time series, under a range of different climate scenarios and time periods. The transition probabilities calculated directly from observations can be perturbed for a range of GWLs using the gradient from Equation (2) for the corresponding grid-cell. Data from weather stations at Santarém, Brazil and Reykjavik, Iceland, have been used to demonstrate the technique based on large and differing parameter responses at their locations (presented in section 3).

First-order transition probabilities will be scaled additively,

$$P_T = P_0 + a_{P_{xy}} \Delta T, \tag{7}$$

where P_T is the new transition probability following a specified global temperature change ΔT relative to the observed period (where the observed transition probability is P_0). Coordinates x and y refer to the GCM grid-cell that encloses the coordinates of the location of the weather station used to calculate P_0. Probabilities have upper (1) and lower (0) limits. If after scaling $P_T > 1$ or $P_T < 0$, the transition probability is truncated below or above the limits at 0.999 and 0.001, respectively. Such truncation is similarly used by Osborn et al. (2016) for precipitation and cloud coverage.

Osborn et al. (2016) suggested that a multiplicative approach is appropriate for pattern scaling shape and scale parameters because they are bounded at zero. Wet-day gamma distribution parameters are therefore scaled multiplicatively,

$$W_T = W_0(1 + a_W \Delta T), \tag{8}$$

where W_T is the new gamma parameter following the global temperature change ΔT relative to the observed period (for which the observation-based gamma parameters are W_0). Once again, the scaled parameters must be constrained to the physically allowed range ($W > 0$). If a parameter falls below 0 following scaling, it will instead be set to an arbitrary small number (i.e., 0.01). We also recommend that prior to application of our method, the suitability of the gamma distribution should be assessed at the site where the observed parameters, W_0, are calculated.

The perturbed transition probabilities, P_T, and wet-day parameters, W_T, can hence be used to generate time series of precipitation under the specified GWLs. This method of synthetic time series generation avoids GCM-induced bias because the starting point is the parameters fit to observations and *only* changes in parameters are taken from the GCM. For a given site, the area-averaged data can vary significantly from the local, weather station scale data. Therefore, using local-scale data perturbed by GCM predicted trends will reduce errors in estimating the local climate.

3 | RESULTS AND DISCUSSION

3.1 | Precipitation parameter response to changing GMST

Change patterns from only one GCM, IPSL-CM6A-LR, are used here to illustrate the implementation of the SPG-PS process. It is nevertheless informative to consider the dominant spatial structures in the results to assess whether they are physical. Spatial responses for P_{00} and P_{11} are shown in Figure 1. Deductions about the transition probabilities, P_{01} and P_{10}, can be drawn from P_{00} and P_{11}, respectively. For visualization purposes, the maximum and minimum transition probability responses are capped at +6% and −6%, respectively, where a value of 6% (−6%) indicates an increase (decrease) of 6 in the transition probability percentage per degree GMST increase (e.g., an increase of 6%·°C^{-1} following a GMST increase of 2°C would correspond to +12% added to the original value, not an addition of 12 percent of the original value). Note that the colour bars have been reversed for P_{11} and P_{00} to indicate increasing wet or dry conditions with consistent colours. Seasons may be referred to by their months, DJF (December, January, February), MAM (March, April, May), JJA (June, July, August) and SON (September, October and November).

Regions with the strongest transition probability response to increased GMST include Central Africa, and regions with monsoon seasons (i.e., the Amazon rainforest, Southeast Asia). For brevity, a summary of the responses and potential implications on the occurrence of precipitation is shown in Table 1.

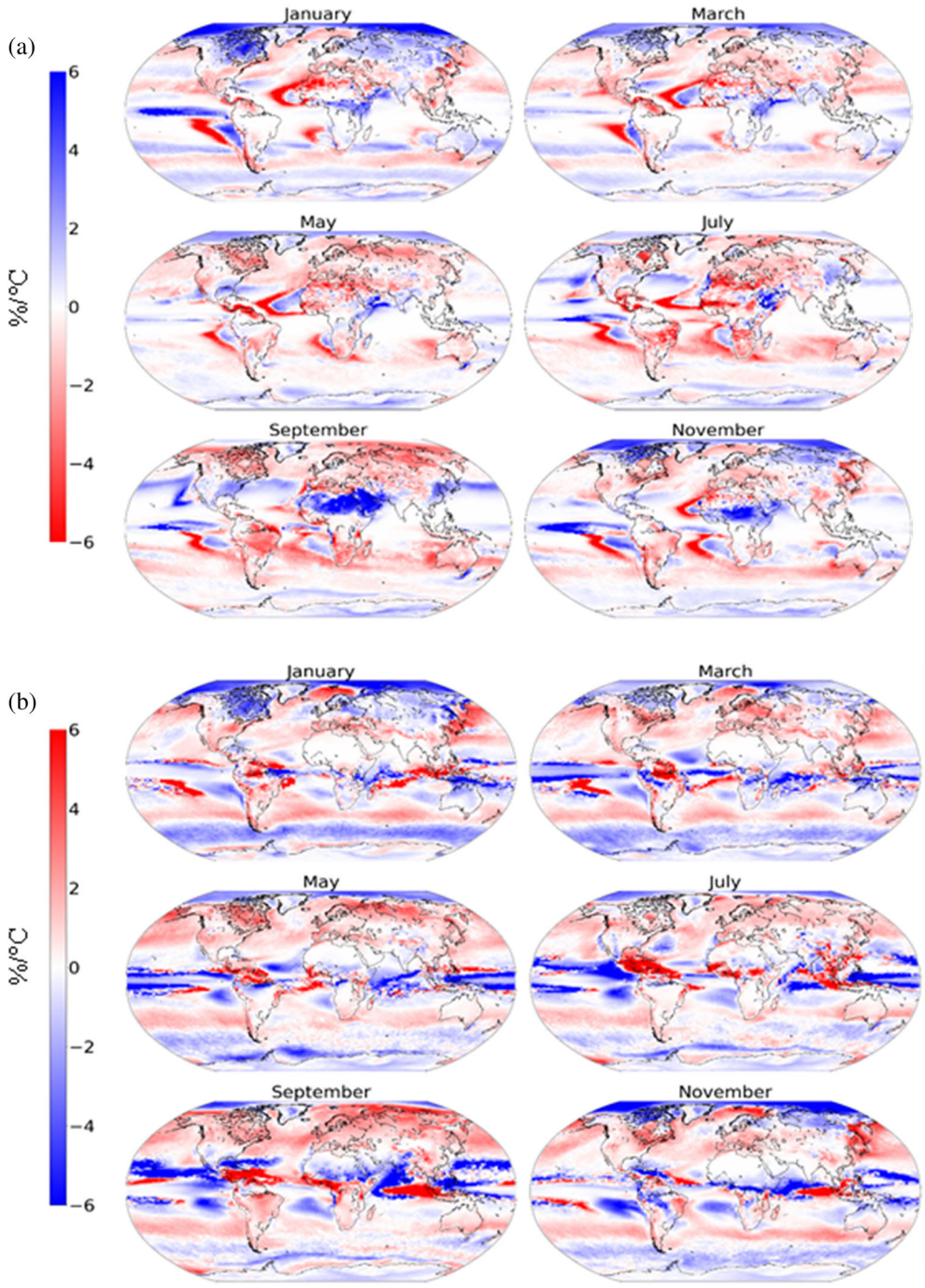

FIGURE 1 Monthly change in P_{11} (a) and P_{00} (b) per degree GMST increase, diagnosed using pooled IPSL-CM6A-LR historical, SSP3-7.0 and SSP5-8.5. Note that every other month has been shown for ease of viewing and due to temporal coherence. All 12 months can be seen in Supporting Information alongside regression R^2 scores (Figures S1 and S2, respectively) [Colour figure can be viewed at wileyonlinelibrary.com]

The linear scaling of transition probabilities with GMST is novel, and the coefficient of determination, R^2, has been determined to evaluate the least-square fit described in Equation (2). R^2 values are typically high in regions where the response signal is strong (see Figures S1 and S2, Supporting Information) and conversely low where the response signal is weaker. P_{11} responses over South America and the high latitudes exemplify this well. Much of Brazil, southern Argentina and Chile have strong P_{11} responses from September to January. Much of high-latitude Europe also has a strong signal, with an accompanying strong R^2. As the P_{11} response decreases towards lower latitudes, so too does the R^2 score. Exceptions to this trend are present over North Africa (December–August) where the occurrence of rainy days is few, and the calculated probabilities are frequently zero. This may indicate regime specific or seasonal performance of the model.

Conversely to the transition probabilities, the wet-day gamma parameter responses are shown as fractional changes per degree warming, where a value of +0.5 indicates an increase of 50% of the original value per degree

TABLE 1 Summarizing responses presented in Figure 1

Region	Parameter		Implications
	P_{11}	P_{00}	
South America	Negative trends over north, east, Amazon rainforest regions; strongest magnitude in April/May	Strong negative response May–October in north, east, Amazon region—typically dry season	Increased dry-day frequency and dry-spell length; increased max CDD, longer dry season (Sörensson et al., 2010)
North America	Positive trends over Canada and Alaska in DJF. Weak trends over contiguous USA; exceptions over east coast in SON and west coast in DJF	Frequent positive trends over many North American regions. Some localized trends in Midwest USA and west coast in July–September	Increased wet-day frequency and spell length in DJF in Canada and Alaska. Slightly increased dry-day frequency across contiguous USA with longer spell-length over western USA
Central America	Localized positive trends from May to June over coastal cells	Large positive trend in Central America, JJA and September	Strong responses during country's wet seasons; increased CDD and reduced wet-day occurrence. Decreased overall precipitation (Ortega et al., 2021; Hidalgo et al., 2013)
Northern Europe and Eurasia	Spatially widespread, positive trends in DJF. Conversely, negative trend shown in JJA. Relatively small in magnitude	Widespread negative trends in DJF. Opposite trends in other months, with localized responses in MAM, September and October over Eurasian subarctic	In DJF, higher frequency and increasing length of wet-spells. Converse in JJA, with higher frequency, and increasing length, of dry-spells
East and Southeast Asia	Little change to transition probabilities during monsoon seasons (e.g., JJA in India and July/August over East Asia)	Positive, high magnitude trends in winter months (DJF) over Korea and north-east China	Fewer wet days, with longer dry spells during DJF in east Asia. Monsoon dynamics governing precipitation patterns results in fewer changes during monsoon seasons in different regions
Middle East	Saudi Arabia, Yemen and Oman have strong positive trends from May to November	Little change in most seasons, though with negative trends from August to September (alongside positive P_{11} trends)	Increased frequency of wet days in what is presently considered dry season (Almazroui et al., 2012)
East and Central Africa	Positive trends from August to January; particularly large spatial coverage in SON	In east Africa, P_{00} response is weaker than P_{11}; negative trends in SON	Increasing number of wet days. Reiterates general consensus regarding a wetter east Africa (Cooper et al., 2008)
West and Southern Africa	Strong negative trends May, JJA (West) and negative trends from June to Oct (Southern)	In the West, P_{00} trends contrast negative P_{11} trends, with positive trends in JJA, September. In southern Africa, positive trends in several months	Increased CDD and decreased CWD in West; reiterates findings of Klutse et al. (2018) regarding a wetter Guinea Coast region as GMST increases. In the south, Increased drought risk and CDD frequency region (Almazroui et al., 2021)

Note: CDD is the no. consecutive dry days per year and CWD is no. consecutive wet days per year. Where relevant, in the "implications" column, references correspond to studies that demonstrate similar findings (see Figures S1 and S2 for changes in P_{11} and P_{00} on a monthly basis).

warming, that is, for a shape parameter of 3 and a response of 0.5, the parameter following 1° of warming becomes 4.5 (i.e., a 50% increase on the original value). Shape and scale parameter changes (per °C) have been capped at ±0.5, and ±0.3, respectively, for visualization purposes only. Responses are spatially coherent and mostly temporally coherent between adjacent months. This indicates that the dependence of these parameters on GMST change can be diagnosed without being dominated by local scale noise.

While interpreting the transition probability responses is intuitive, inferring changes to the wet-day

parameters is less straightforward since unlike P_{11} and P_{00}, shape and scale parameters are not independent of each other and it is their combined impact that determines, for example, how likely an extreme value is. Nevertheless, a reduction in shape parameter leads to a more positively skewed gamma distribution (i.e., less consistent precipitation amounts) while a large increase in shape from an initial value of 1 will adjust the distribution from an exponential-type character towards a more bell-shaped function. Here, shape responses will be discussed in absence of any changes in the scale parameter, with the breadth of all distributions (irrespective of shape) also determined by changes to the scale parameter which will be presented later. For the case studies, we combine changes in the shape and scale parameters to determine the resulting distribution for future climates.

Changes to the shape and scale parameters (shown in Figure 2, with all months shown in Figures S3 and S4)

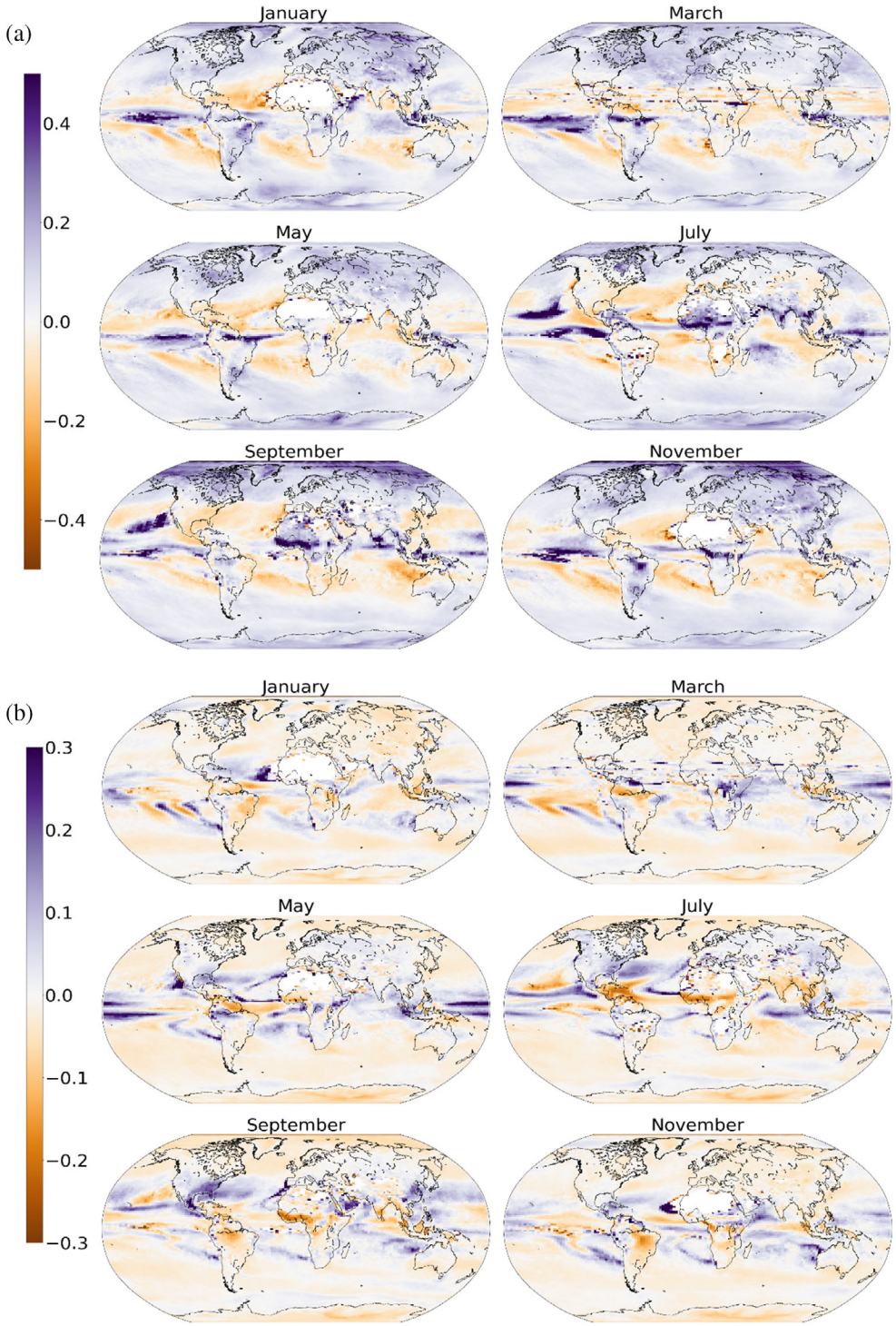

FIGURE 2 Fractional change in wet-day (a) shape and (b) scale parameters per degree GMST increase, diagnosed from IPSL-CM6A-LR historical, SSP3-7.0 and SSP5-8.5. Note that every other month has been shown for ease of viewing and due to temporal coherence. All 12 months can be seen in Figures S3 and S4, respectively [Colour figure can be viewed at wileyonlinelibrary.com]

TABLE 2 Summarizing responses presented in Figure 2 (see Figures S3 and S4 for changes in shape and scale on a monthly basis)

Region	Parameter		Potential implications
	Shape (α)	Scale (β)	
Africa	Widespread positive trend from July to September in West and Central Africa	Negative trend present in JJA and September (Central and West)	Strongest increases in α and β coincide with strong changes in P_{00} and P_{11}. Net effect is difficult to determine; agrees with Cooper et al. (2008) with respect to uncertainties in modelling precipitation in West Africa
South America	Amazon regions show strong positive trends in February, MAM. Southeast Brazil has large increases all year; conversely, decreases present east coast of Brazil from August to October	Amazon and central Brazil show negative trends in SON; coinciding with dry season	Already in the dry season, days with precipitation may shift to even smaller amounts; exacerbating dry conditions
Southeast Asia and India	Spatially localized, strong positive responses in several months (e.g., August; see Figure S3)	Weak positive trends	A shift towards smaller precipitation amounts (less skew). In combination with increasing P_{00}, the region may become drier
China	Widespread decreases in the east in JJA and September	Eastern China demonstrates trends of a different sign to Southeast Asia; moderate positive trends in JJA, September	Strongest trends in α and β occur during wet season in China; large implications to overall mean daily precipitation distribution, potentially with more variability; though dependent on relative strength of parameter changes
Central and North America	Typically consistent with global slight positive trends. Widespread decreases in the east in JJA and September	Seasonally varying responses. Positive trend focussed on eastern USA, peaking in magnitude in September. Central America has positive trend JJA	Greater variability in daily precipitation amounts
Europe and Eurasia	Responses reflect changes at similar latitudes in North America. Strongest response in the high latitudes, with changes reflecting widespread global increases	Weaker trends; widespread negative, with some positive responses over continental regions in JJA	More variability, with precipitation distributions changing most drastically towards the high latitudes

are seemingly less affected by the seasons than the transition probabilities. All months show slight fractional increases to the shape parameter over most land surface areas. Most regions do not show strong or seasonal changes to shape parameter response, with noteworthy exceptions in Africa and South America. A summary of the strongest responses are presented in Table 2.

3.2 | Application of responses to a stochastic precipitation generator

To demonstrate the application of the response patterns to observed data, synthetic precipitation time series at two weather stations for a wide range of GWLs has been produced using PS-perturbed parameters following Equations (7) and (8). Santarém, Brazil and Reykjavik, Iceland have been chosen as case study locations for reasons provided in section 2. Global Summary of the Day data, provided by the National Centers for Environmental Information (NCEI), have been used for Santarém (dataset identifier: NCEI DSI 3505, accessible from https://www.ncei.noaa.gov/access/metadata/landing-page/bin/iso?id=gov.noaa.ncdc:C00516) and the European Climate Assessment & Dataset (ECAD) for Reykjavik (Klein Tank et al., 2002). Note that this section aims to demonstrate strengths and the application of the combined SPG-PS approach in the construction of local-scale time series at

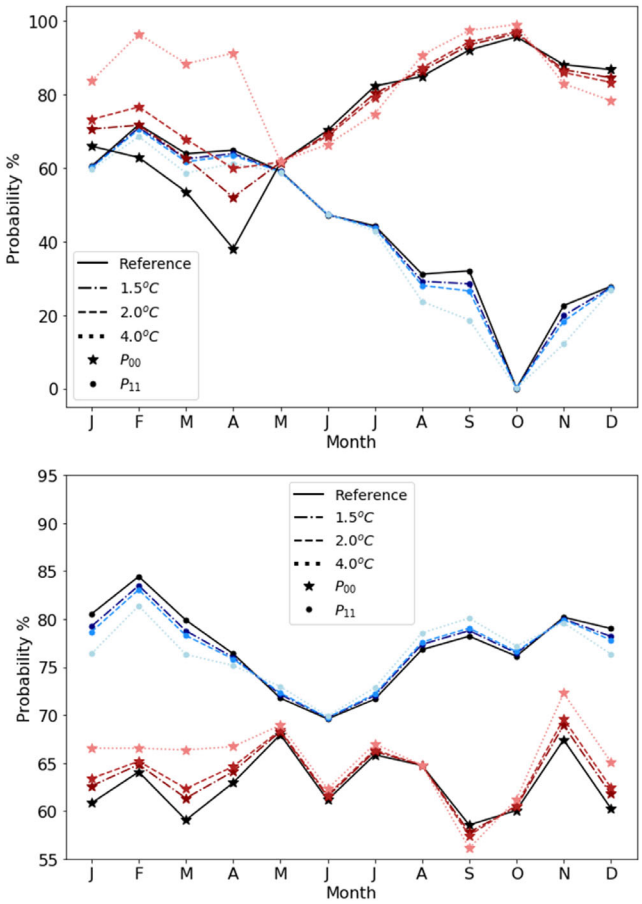

FIGURE 3 Transition probabilities for all months at Santarém (top) and Reykjavik (bottom) for the reference period and at GWLs 1.5, 2.0 and 4.0°C [Colour figure can be viewed at wileyonlinelibrary.com]

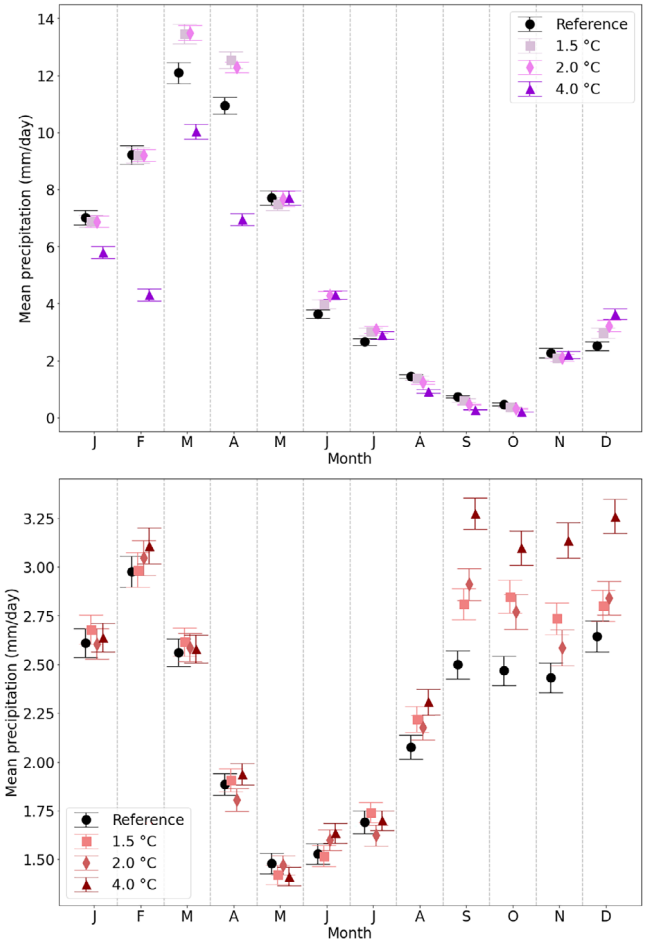

FIGURE 4 Mean daily precipitation (mm·day^{-1}) at Santarém (top) and Reykjavik (bottom), at different GWLs. Error bars show the standard error in the mean [Colour figure can be viewed at wileyonlinelibrary.com]

a range of GWLs and *not* a comprehensive assessment of the future climate at the two case study locations.

Observed parameters (P_O and W_O in Equations (7) and (8)) have been calculated directly from the weather station records. One hundred years of precipitation is simulated using the precipitation generator, configured with the observed parameters. This is hereafter referred to as the "reference" period (representative of the observed climate). The IPSL-CM6A-LR GCM grid cell that encompasses the geographical coordinates of each weather station has been used to determine $a_{P_{xy}}$ and $a_{W_{xy}}$ (in Equations (2) and (6)). Parameters have been scaled using GMST increases relative to the 1850–1900 mean for a range of GWLs (from 0.8 to 5.0°C) easily implemented via term ΔT in Equations (7) and (8) highlighting a strength of the combined SPG-PS approach.

The time periods covered by the observed data records used to estimate the reference SPG parameters differs between the two sites. The mean observed GMST anomaly for each reference period is calculated using the HadCRUT5 dataset (Morice et al., 2021) relative to the 1850–1900 mean. At Santarém, the GMST anomaly is 0.78°C for the time period with observations (1990–2020) and 0.56°C at Reykjavik (1970–2020). The difference between the reference GMST and each GWL is calculated and substituted into ΔT in Equations (7) and (8) to determine P_T and W_T, respectively. The GWL scaled SPG parameters are then used to produce further 100-year time series for both sites. Figure 3 shows scaled transition probabilities, P_T, at Santarém and Reykjavik at three example GWLs (1.5, 2.0 and 4.0°C). At Reykjavik (bottom panel, Figure 3), changes to the transition probabilities are relatively constant during JJA. Changes are greatest during DJF, with decreases to P_{11} and increases to P_{00}. At Santarém (top panel, Figure 3), perturbed transition probabilities show large increases to P_{00} from January to April, followed by relatively small changes in both P_{11} and P_{00} for the rest of the year.

With respect to mean daily precipitation amounts, following the scaling of P_T and W_T, Santarém shows large decreases at GWL 4°C in January–April (see Figure 4),

with minimal change in all other months. Strong transition probability responses drive this decreased precipitation; the mean number of wet days per year decreases from 109 during the reference period to 75 by GWL 4°C, with the changes loaded to the first third of the year (e.g., April; decreasing from 21 to 11 wet days per month, at GWL 4°C). While decreases in mean daily precipitation are present at higher GWLs (in March and April), there are *increases* in mean precipitation at lower GWLs. This is driven by reduced skew and higher mean wet-day precipitation amounts as a result of changes in the wet-day gamma distribution. This indicates that although there is a large reduction in wet-day occurrence, on days where there is precipitation, greater amounts with more variability may be expected.

Changes to precipitation in March and April are in stark contrast with May (and indeed the remainder of the year, constituting the local dry season), where transition probability and wet-day gamma parameter responses are close to zero resulting in little change to the number of, and precipitation on, wet days. The reduction in precipitation at a GWL of 4°C for the first quarter of the year agrees with changes discussed in literature based on a wider range of GCMs. For example, Sörensson et al. (2010) found increases to CDD, alongside significant decreases in DJF and MAM total precipitation in the Amazon basin. Averaging the simulated precipitation over these seasons agrees with these findings.

Conversely, mean daily precipitation at Reykjavik is projected to increase in several months (e.g., September–December, all GWLs). Alongside increases in mean daily precipitation, changes to the variability are present. Increases in mean daily precipitation are accompanied by an increase of 11.9% in the standard deviation of daily values (averaged from September to December, between the reference period and 4.0°C), with the largest increase in December (15.5%). Wet days per month remain relatively unchanged (i.e., from 18.1 during the reference period to 18.4 at GWL 4°C) during these months. This change in variability is therefore caused by changes to the wet-day precipitation distributions, and not the change in wet or dry day frequency. Changes in variability may therefore result in an increased number of *very* wet days, resulting in a potentially increased risk of extreme precipitation.

Changes to the mean precipitation and the number of wet days per month from May to July (the driest months) are much smaller. Transition probabilities during these months are approximately constant (Figure 3). Changes to the distribution of wet-day precipitation are thus not large enough to affect the mean daily precipitation over these months. However, from January to April the dry-day probability does slightly increase (i.e., with increases in P_{00} and decreases in P_{11}). Despite this, the precipitation total in January, March, and April remains fairly unchanged between the GWLs because fewer dry days are offset by projected increases in January to May mean wet-day precipitation (by an average of 11.9% for GWL 4°C in comparison to the reference period). Therefore, despite decreases in the number of wet days per month, the precipitation that may be expected on any wet day during this period is larger. The percentage change is largest in February (15.7% by 4.0°C) where the mean daily precipitation increases at each GWL, despite the decreases to the wet-day frequency.

3.2.1 | Using the pattern scaled observations to assess extremes

A common use of stochastic precipitation generators is in the robust assessment of extreme events and the ability to efficiently construct long, temporally consistent time series is a prime advantage of these tools (Furrer & Katz, 2008; Senemov, 2008). The annual maximum 5-day precipitation total is a metric that has been used in impact and attribution assessments (recent examples include Pińskwar et al. (2019) and Paik et al. (2020)) to detect changes in extreme precipitation. Here, 5-day precipitation totals are calculated (with days overlapping, such that precipitation is summed on Day 1–5, Day 2–6 and so on) and the annual maximum recorded for each of the 100 years simulated series.

At Santarém, the mean annual maximum 5-day precipitation is decreasing at higher GWLs, owing to the decreases in mean daily precipitation wet seasons (shown in Figure 4). However, up until GWL 2.0°C the median annual maximum 5-day precipitation increases, along with the range and standard deviation. This is due to competing effects between changes in the transition probabilities and the gamma parameters, thus resulting in a nonlinear response to increasing GMST. During the reference period, the maximum 5-day precipitation typically occurred during March. However, as GMST increases, this maximum instead falls in April or May (not shown), altogether indicating a change in the seasonal precipitation, with the outliers evolving such that they mirror the median. Conversely in Reykjavik, there is slight a positive trend in the annual maximum 5-day precipitation, with the mean increasing from 51.6 to 58.1 mm approximately linearly. In both locations, outliers are typically present at the upper end of the distribution (Figure 5).

Another metric that can be considered is the distributions of wet and dry spell lengths (WSL and DSL, respectively), and particularly the extremes of these which are relevant for potential flooding and droughts. At

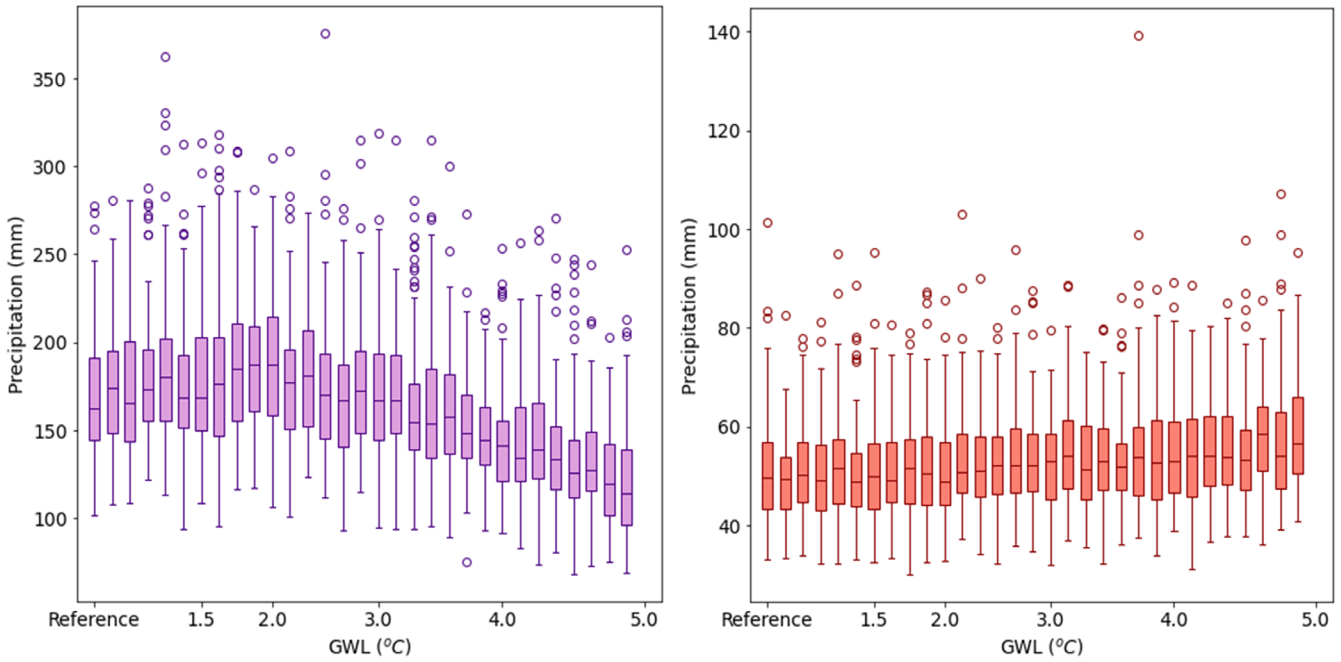

FIGURE 5 Boxplots showing the annual maximum 5-day precipitation from the reference period to 5.0°C GWL at Santarém (left) and Reykjavik (right). Candles show the medians (horizontal line) and interquartile ranges for the annual maximum 5-day precipitation (each candle has sample size 100). Circles outside of the candles are outliers [Colour figure can be viewed at wileyonlinelibrary.com]

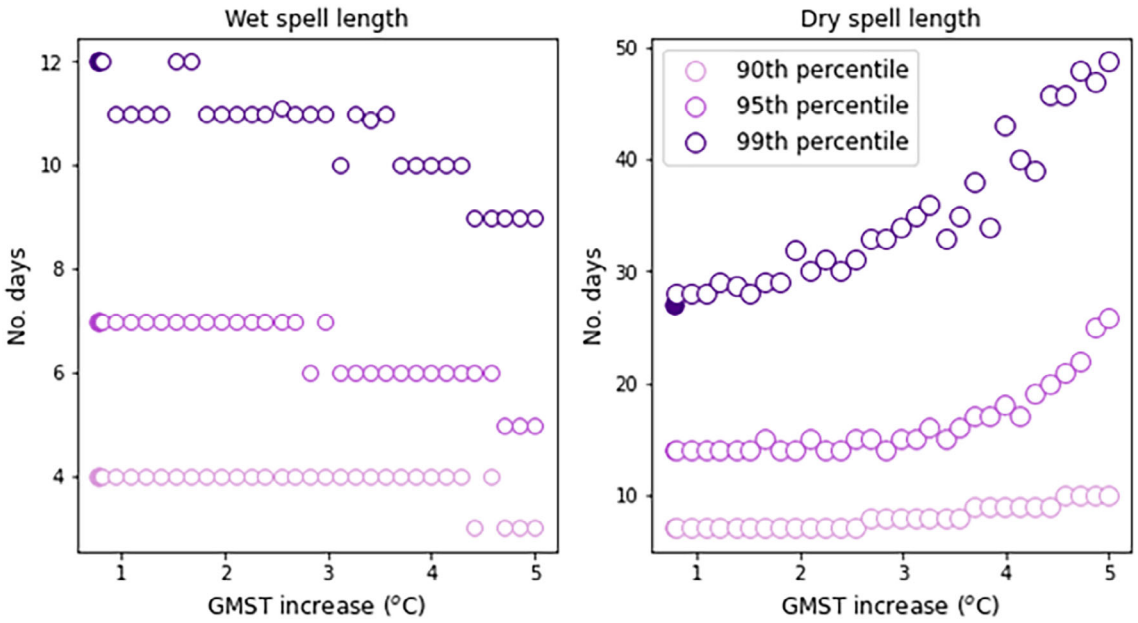

FIGURE 6 WSL and DSL extreme percentiles at Santarém. Filled circles represent the reference period [Colour figure can be viewed at wileyonlinelibrary.com]

Reykjavik, changes to the WSL and DSL distributions are minimal (not shown). However, at Santarém there are large changes to the DSL distribution (shown in Figure 6). While the 90th percentile of DSL increases only slightly with GMST, the 99th percentile rapidly increases with GMST. This indicates a shift to a heavier tailed distribution with an increased change of very long dry spells which would contribute to drought severity. From the reference period to a GWL of 5.0°C, the 99th DSL percentile has almost doubled (from 27 to 48 days) resulting in a 99th percentile that lasts over a full calendar month.

Convenient production, and analysis, of the two metrics shown here from the source SPG-PS data demonstrates the strength of the approach, though there are many further strengths that have not been demonstrated here. For example. further analyses may include extreme value analysis (EVA), assessment of drought and flood return periods, or calculation of further extreme indices. While one realization of a 100-year time series at each GWL has been produce here, it is computationally economic to simulate several realizations of the same GWL, ultimately driven by different GCM patterns and forcing scenarios, thus providing a robust tool with which to capture local-scale climate uncertainty.

4 | CONCLUSION

We have described a novel approach applying PS to a SPG in order to produce daily precipitation series accounting for changes in both Markov-chain properties and a two-parameter gamma-distribution of wet day amounts. The response of the Markov chain transition probabilities, P_{11} and P_{00}, and wet-day gamma distribution parameters (shape and scale), to changing GMST have been diagnosed using pooled ensemble members of historical, SSP3-7.0 and SSP5-8.5 simulations produced by IPSL-CM6A-LR. These response patterns have been diagnosed globally and have been applied to weather-station scale data to illustrate the approach in full and highlight strengths of the combined SPG-PS, for a selection of GWLs.

We find that in regions of strong transition probability response, linear regression R^2 scores are generally high, with spatially concentrated exceptions. Transition probability responses agree qualitatively with studies based on a wider range of GCMs, improving confidence in the physical interpretations behind the patterns. The response of the transition probabilities to changing GMST is seasonally varying, with the strongest land responses generally across Africa, South America and Southeast Asia. In the Northern Hemisphere, similar latitudes tend to show similar responses in magnitude, direction, and spatial coverage. This is most noticeable with P_{11} where winter months show widespread increases with GMST, and summer months show prevalent decreases. The response of the wet-day gamma parameters to changing GMST are less intuitive to interpret, and in most locations, seasonally varying patterns are not present. However, once again, Africa and South America show some of the largest responses, indicating changes to the precipitation nature in these regions, in combination with strong transition probability response.

Applying PS to a SPG utilizes the advantages of both techniques and unifies them into a single methodology. For example, PS provides a method for the construction of a wide range of climate scenarios to capture a range of uncertainties with computational efficiency and, as we show here, an efficient technique to derive SPG parameters for a variety of GWLs (0.8–5.0°C in this case). Meanwhile, SPGs can efficiently produce several realizations of long, local-scale time series, that are suitable for impact assessments, and which can be statistically representative of the weather at the site used for calibration. This study has utilized responses to GMST change to perturb observed SPG parameters at Santarém and Reykjavik, producing time series at a scale appropriate for impact assessors and as inputs to hydrological, agricultural and ecological models. We have produced time series that, at high GWLs, show large reductions in local wet-season precipitation at Santarém, largely driven by changes in the transition probabilities. Conversely, increases to both the mean and standard deviation in wet-season precipitation is projected at Reykjavik, driven by changes to both the transition probabilities and the wet-day gamma parameters. We have also shown how the SPG-PS approach can conveniently study extreme metrics such as (but not limited to) annual 5-day maximum precipitation and the distribution of wet and dry spell lengths.

In whole, our study demonstrates the capabilities of the combined SPG-PS approach to emulate future scenarios which can be readily extended to emulate further permutations of scenarios, time periods, and GMST increases not simulated by GCMs or shown here. Finally, and importantly, the SPG-PS framework also allows for the incorporation of GCM-dependant differences in the responses of the parameters to increasing GMST via diagnosing, and then interchanging with the afore-mentioned factors, response patterns from alternative GCMs. As a result, a wider range of realizations for specific global warming levels can be constructed to better explore and account for a range of uncertainties for consideration in robust adaptation plans.

It is important to note that different GCMs will likely produce differing responses of the parameters to increasing GMST. Through diagnosing similar response patterns from alternative GCMs, a wider range of realizations for specific global warming levels can be constructed to better explore and account for a range of uncertainties for consideration in robust adaptation plans.

AUTHOR CONTRIBUTIONS

Sarah Wilson Kemsley: Writing – original draft; investigation; conceptualization; methodology. **Timothy J. Osborn:** Methodology; writing – review and editing; supervision; conceptualization. **Stephen R. Dorling:** Writing – review and editing; supervision. **Craig Wallace:** Writing – review and editing; supervision.

ACKNOWLEDGEMENTS

The research presented in this article was supported by the Natural Environment Research Council, EnvEast Doctoral Training Partnership (grant number NE/S007334/1) and CASE partner Atkins and was carried out on the High Performance Computing Cluster supported by the Research and Specialist Computing Support service at the University of East Anglia. We thank the anonymous reviewers for their insightful comments and suggestions which have improved the manuscript.

CONFLICT OF INTEREST STATEMENT

The authors declare no conflicts of interest.

DATA AVAILABILITY STATEMENT

The data that support the findings of this study are available from the corresponding author upon reasonable request.

ORCID

Sarah Wilson Kemsley https://orcid.org/0000-0002-7652-5060

REFERENCES

Almazroui, M., Islam, M.N., Jones, P.D., Athar, H. & Rahman, M.A. (2012) Recent climate change in the Arabian Peninsula: seasonal rainfall and temperature climatology of Saudi Arabia for 1979–2009. *Atmospheric Research*, 111, 29–45. Available from: https://doi.org/10.1016/j.atmosres.2012.02.013

Almazroui, M., Saeed, F., Saeed, S., Ismail, M., Ehsan, M.A., Islam, M.N. et al. (2021) Projected changes in climate extremes using CMIP6 simulations over SREX regions. *Earth Systems and Environment*, 5, 481–497. Available from: https://doi.org/10.1007/s41748-021-0250-5

Boucher, O., Servonnat, J., Albright, A.L., Aumont, O., Balkanski, Y., Bastrikov, V. et al. (2020) Presentation and evaluation of the IPSL-CM6A-LR climate model. *Journal of Advances in Modeling Earth Systems*, 12, e2019MS002010. Available from: https://doi.org/10.1029/2019MS002010

Chen, J. & Brissette, F. (2014) Stochastic generation of daily precipitation amounts: review and evaluation of different models. *Climate Research*, 59(3), 189–206. Available from: https://doi.org/10.3354/cr01214

Cooper, P.J.M., Dimes, J., Rao, K.P.C., Shapiro, B., Shiferaw, B. & Twomlow, S. (2008) Coping better with current climatic variability in the rain-fed farming systems of sub-Saharan Africa: an essential first step in adapting to future climate change? *Agriculture, Ecosystems & Environment*, 126, 24–35. Available from: https://doi.org/10.1016/j.agee.2008.01.007

Furrer, E.M. & Katz, R.W. (2008) Improving the simulation of extreme precipitation events by stochastic weather generators. *Water Resources Research*, 44, W12439. Available from: https://doi.org/10.1029/2008WR007316

Groisman, P.Y., Karl, T.R., Easterling, D.R., Knight, R.W., Jamason, P.F., Hennessy, K.J. et al. (1999) Changes in the probability of heavy precipitation: important indicators of climatic change. *Climatic Change*, 42, 243–283. Available from: https://doi.org/10.1023/A:1005432803188

Haarsma, R.J., Roberts, M.J., Vidale, P.L., Catherine, A., Bellucci, A., Bao, Q. et al. (2016) High Resolution Model Intercomparison project (HighResMIP v1.0) for CMIP6. *Geoscientific Model Development*, 9, 4185–4208. Available from: https://doi.org/10.5194/gmd-9-4185-2016

Hidalgo, H.G., Amador, J.A., Alfaro, E.J. & Quesada, B. (2013) Hydrological climate change projections for Central America. *Journal of Hydrology*, 495, 94–112. Available from: https://doi.org/10.1016/j.jhydrol.2013.05.004

IPCC. (2021) The physical science basis. Contribution of working group I to the sixth assessment report of the Intergovernmental Panel on Climate Change. In: Masson-Delmott, V., Zhai, P., Pirani, A., Connors, S.L., Péan, C., Berger, S. et al. (Eds.) *Climate change 2021*. Cambridge and New York, NY: Cambridge University Press.

Jimoh, O.D. & Webster, P. (1996) The optimum order of a Markov chain model for daily rainfall in Nigeria. *Journal of Hydrology*, 185, 45–69. Available from: https://doi.org/10.1016/S0022-1694(96)03015-6

Jones, C.D., Hughes, J.K., Bellouin, N., Hardiman, S.C., Jones, G.S., Knight, J. et al. (2011) The HadGEM2-ES implementation of CMIP5 centennial simulations. *Geoscientific Model Development*, 4, 543–570. Available from: https://doi.org/10.5194/gmd-4-543-2011

Jones, P.D., Harpham, C., Burton, A. & Goodess, C.M. (2016) Downscaling regional climate model outputs for the Caribbean using a weather generator. *International Journal of Climatology*, 36, 4141–4163. Available from: https://doi.org/10.1002/joc.4624

Katz, R.W. & Brown, B.G. (1992) Extreme events in a changing climate: variability is more important than averages. *Climatic Change*, 21, 289–302. Available from: https://doi.org/10.1007/BF00139728

Klein Tank, A.M.G., Wijngaard, J.B., Können, G.P., Böhm, R., Demarée, G., Gocheva, A. et al. (2002) Daily dataset of 20th-century surface air temperature and precipitation series for the European climate assessment. *International Journal of Climatology*, 22, 1441–1453. Available from: https://doi.org/10.1002/joc.773

Klutse, N.A.B., Ajayi, V.O., Gbobaniyi, E.O., Egbebiyi, T.S., Kouadio, K., Nkrumah, F. et al. (2018) Potential impact of 1.5°C and 2°C global warming on consecutive dry and wet days over West Africa. *Environmental Research Letters*, 13, 055013. Available from: https://doi.org/10.1088/1748-9326/aab37b

Lynch, C., Hartin, C., Bond-Lamberty, B. & Kravitz, B. (2017) An open-access CMIP5 pattern library for temperature and precipitation: description and methodology. *Earth System Science Data*, 9, 281–292. Available from: https://doi.org/10.5194/essd-9-281-2017

Maraun, D., Wetterhall, F., Ireson, A.M., Chandler, R.E., Kendon, E.J., Widmann, M. et al. (2010) Precipitation downscaling under climate change: recent developments to bridge the gap between dynamical models and the end user. *Reviews of Geophysics*, 48, RG3003. Available from: https://doi.org/10.1029/2009RG000314

Martinez-Villalobos, C. & Neelin, J.D. (2019) Why do precipitation intensities tend to follow gamma distributions? *Journal of Atmospheric Sciences*, 76, 3611–3631. Available from: https://doi.org/10.1175/JAS-D-18-0343.1

May, W. (2012) Assessing the strength of regional changes in near-surface climate associated with a global warming of 2°C. *Climatic Change*, 110, 619–644. Available from: https://doi.org/10.1007/s10584-011-0076-y

Mitchell, T.D. (2003) Pattern scaling. An examination of the accuracy of the technique for describing future climates. *Climatic Change*, 60, 217–242. Available from: https://doi.org/10.1023/A:1026035305597

Morice, C.P., Kennedy, J.J., Rayner, N.A., Winn, J.P., Hogan, E., Killick, R.E. et al. (2021) An updated assessment of near-surface temperature change from 1850: the HadCRUT5 data set. *Journal of Geophysical Research: Atmospheres*, 126, e2019JD032361. Available from: https://doi.org/10.1029/2019JD032361

O'Neill, B.C., Tebaldi, C., Van Vuuren, D.P., Eyring, V., Friedlingstein, P., Hurtt, G. et al. (2016) The Scenario Model Intercomparison project (ScenarioMIP) for CMIP6. *Geoscientific Model Development*, 9, 3461–3482. Available from: https://doi.org/10.5194/gmd-9-3461-2016

Ortega, G., Arias, P.A., Villegas, J.C., Marquet, P.A. & Nobre, P. (2021) Present-day and future climate over central and South America according to CMIP5/CMIP6 models. *International Journal of Climatology*, 41, 6713–6735.

Osborn, T.J. (1997) Areal and point precipitation intensity changes: implications for the application of climate models. *Geophysical Research Letters*, 24, 2829–2832. Available from: https://doi.org/10.1029/97GL02976

Osborn, T.J., Wallace, C.J., Harris, I.C. & Melvin, T.M. (2016) Pattern scaling using ClimGen: monthly-resolution future climate scenarios including changes in the variability of precipitation. *Climatic Change*, 134, 353–369. Available from: https://doi.org/10.1007/s10584-015-1509-9

Osborn, T.J., Wallace, C.J., Lowea, J.A. & Bernie, D. (2018) Performance of pattern-scaled climate projections under high-end warming. Part I: surface air temperature over land. *Journal of Climate*, 31, 5667–5680. Available from: https://doi.org/10.1175/JCLI-D-17-0780.1

Paik, S., Min, S.K., Zhang, X., Donat, M.G., King, A.D. & Sun, Q. (2020) Determining the anthropogenic greenhouse gas contribution to the observed intensification of extreme precipitation. *Geophysical Research Letters*, 47, e2019GL086875. Available from: https://doi.org/10.1029/2019GL086875

Pińskwar, I., Choryński, A., Graczyk, D. & Kundzewicz, Z.W. (2019) Observed changes in extreme precipitation in Poland: 1991–2015 versus 1961–1990. *Theoretical and Applied Climatology*, 135, 773–787. Available from: https://doi.org/10.1007/s00704-018-2372-1

Riahi, K., van Vuuren, D.P., Kriegler, E., Edmonds, J., O'Neill, B.C., Fujimori, S. et al. (2017) The Shared Socioeconomic Pathways and their energy, land use, and greenhouse gas emissions implications: an overview. *Global Environmental Change*, 42, 153–168. Available from: https://doi.org/10.1016/j.gloenvcha.2016.05.009

Richardson, C.W. & Wright, D.A. (1984) *WGEN: a model for generating daily weather variables. ARS-8.* Washington, DC: United States Department of Agriculture, Agriculture Research Service, 83.

Ruosteenoja, K., Tuomenvirta, H. & Jylhä, K. (2007) GCM-based regional temperature and precipitation change estimates for Europe under four SRES scenarios applying a super-ensemble pattern-scaling method. *Climatic Change*, 81, 193–208. Available from: https://doi.org/10.1007/s10584-006-9222-3

Santer, B.D., Wigley, T.M.L., Schlesinger, M.E. & Mitchell, J.F.B. (1990) *Developing climate scenarios from equilibrium GCM results*. Hamburg, Germany: Max-Planck-Institut für Meteorologie.

Schoof, J.T. & Pryor, S.C. (2008) On the proper order of Markov chain model for daily precipitation occurrence in the contiguous United States. *Journal of Applied Meteorology and Climatology*, 47, 2477–2486. Available from: https://doi.org/10.1175/2008JAMC1840.1

Semenov, M.A. & Barrow, E.M. (2002) *A stochastic weather generator for use in climate impact studies*. Hertforshire UK: User Manual.

Semenov, M.A., Brooks, R., Barrow, E. & Richardson, C. (1998) Comparison of the WGEN and LARS-WG stochastic weather generators for diverse climates. *Climate Research*, 10, 95–107. Available from: https://doi.org/10.3354/cr010095

Semenov, V.A. & Bengtsson, L. (2002) Secular trends in daily precipitation characteristics: greenhouse gas simulation with a coupled AOGCM. *Climate Dynamics*, 19, 123–140. Available from: https://doi.org/10.1007/s00382-001-0218-4

Senemov, M.A. (2008) Simulation of extreme weather events by a stochastic weather generator. *Climate Research*, 35, 203–212. Available from: https://doi.org/10.3354/cr00731

Seneviratne, S.I., Zhang, X., Adnan, M., Badi, W., Dereczynski, C., Di Luca, A. et al. (2021) Weather and climate extreme events in a changing climate. In: Masson-Delmott, V., Zhai, P., Pirani, A., Connors, S.L., Péan, C., Berger, S. et al. (Eds.) *Climate change 2021: the physical science basis. Contribution of working group I to the Sixth Assessment Report of the Intergovernmental Panel on climate change*, Vol. 46. Cambridge and New York, NY: Cambridge University Press, pp. 1513–1766. Available from: https://doi.org/10.1029/2018GL080768

Sörensson, A.A., Menéndez, C.G., Ruscica, R., Alexander, P., Samuelsson, P. & Willén, U. (2010) Projected precipitation changes in South America: a dynamical downscaling within CLARIS. *Meteorologische Zeitschrift*, 19, 347–355. Available from: https://doi.org/10.1127/0941-2948/2010/0467

Tebaldi, C. & Arblaster, J.M. (2014) Pattern scaling: its strengths and limitations, and an update on the latest model simulations. *Climatic Change*, 122, 459–471. Available from: https://doi.org/10.1007/s10584-013-1032-9

Tebaldi, C., Debeire, K., Eyring, V., Fischer, E., Fyfe, J., Friedlingstein, P. et al. (2021) Climate model projections from the Scenario Model Intercomparison project (ScenarioMIP) of CMIP6. *Earth System Dynamics*, 12, 253–293. Available from: https://doi.org/10.5194/esd-12-253-2021

van Vuuren, D.P., Edmonds, J., Kainuma, M., Riahi, K., Thomson, A., Hibbard, K. et al. (2011) The representative concentration pathways: an overview. *Climatic Change*, 109, 5–31. Available from: https://doi.org/10.1007/s10584-011-0148-z

Wilby, R.L. & Wigley, T.M.L. (2002) Future changes in the distribution of daily precipitation totals across North America.

Geophysical Research Letters, 29, 39-1–39-4. Available from: https://doi.org/10.1029/2001GL013048

Wilks, D.S. (1999) Multisite downscaling of daily precipitation with a stochastic weather generator. *Climate Research*, 11, 125–136. Available from: https://doi.org/10.3354/cr011125

Wilks, D.S. (2010) Use of stochastic weather generators for precipitation downscaling. *Wiley Interdisciplinary Reviews: Climate Change*, 1, 898–907. Available from: https://doi.org/10.1002/wcc.85

Wilks, D.S. (2011) *Statistical methods in the atmospheric sciences*. Elsevier: Academic Press.

Wilson Kemsley, S., Osborn, T.J., Dorling, S.R., Wallace, C. and & Parker, J. (2021) Selecting Markov chain orders for generating daily precipitation series across different Köppen climate regimes. *International Journal of Climatology*, 41, 6223–6237.

Wu, P., Wood, R., Ridley, J. & Lowe, J. (2010) Temporary acceleration of the hydrological cycle in response to a CO_2 rampdown. *Geophysical Research Letters*, 37, 12705. Available from: https://doi.org/10.1029/2010GL043730

SUPPORTING INFORMATION

Additional supporting information can be found online in the Supporting Information section at the end of this article.

How to cite this article: Kemsley, S. W., Osborn, T. J., Dorling, S. R., & Wallace, C. (2023). Pattern scaling the parameters of a Markov-chain gamma-distribution daily precipitation generator. *International Journal of Climatology*, 1–16. https://doi.org/10.1002/joc.8320